This is a preprint, the final version is subject to change, of the American Mineralogist (MSA)
Cite as Authors (Year) Title. American Mineralogist, in press.
(DOI will not work until issue is live.) DOI: http://dx.doi.org/10.2138/am-2015-4998

Atom probe tomography of isoferroplatinum

Stephen W. Parman[1], David R. Diercks[2], Brian P. Gorman[2], Reid F. Cooper[1]

[1] Department of Geological Sciences, Brown University, Providence, RI 02912

[2] Colorado Center for Advanced Ceramics, Colorado School of Mines, Golden, CO 80401

ABSTRACT

Here we apply the relatively new analytical technique of atom probe tomography (APT) to a naturally occurring isoferroplatinum grain (Pt_3Fe) from northern California in order to constrain its origin and the nanoscale distribution of trace elements within the grain. Each analysis detected the positions of 10 million atoms in 3 dimensions with sub-nanometer spatial resolution. The (111) atomic planes are clearly resolved and their orientation was confirmed by electron backscatter diffraction (EBSD). The elemental concentrations of all elements (Pt, Fe, Ir, Ni, Rh, Ru and Cu) determined from the APT mass/charge spectra are within 2 standard deviations of electron microprobe analysis (EMPA) of the grain. The isotopic abundances determined by APT matches NIST standard compositions over a wide range of concentrations, down to 100 ppmw. Nanoscale areas free of minor and trace elements are present throughout the sample. These could be due to the random distribution of atoms. Alternatively, the Pt-Fe phase diagram indicates that order-disorder precipitates of an $L1_2$ structure could have formed as the isoferroplatinum cooled from magmatic temperatures (Nose et al, 2013). The trace element free areas could be such precipitates, which would support a high-temperature

igneous origin for the isoferroplatinum, rather than formation during low-temperature serpentinization. The results highlight the unique capabilities of APT and the potential utility of knowing the location and identity of atoms in nanometric volumes.

keywords: atom probe tomography, isoferroplatinum, platinum group alloy, precipitate, order-disorder, core-shell

INTRODUCTION

Naturally occurring alloys of Fe with platinum group elements (PGE = Pt, Re, Ru, Rh, Os and Ir) are collectively named platinum group alloys (PGA) and are formed in a range of geological environments (Cabri et al., 1996; Harris and Cabri, 1991). One of the most common localities of PGA is in ophiolites, where they are typically found in placer chromite (black sand) deposits, derived from weathering of the surrounding ultramafic rocks. The high melting temperatures of PGA (>2000°C) and reduced compositions led some researchers to conclude these metals were derived from the Earth's core (Bird and Bassett, 1980; Bird et al., 1999). Subsequent studies have suggested PGA are formed in the upper mantle or crust and are ultimately derived from sulfides, which have high PGE concentrations. One hypothesis is that they are formed during weathering of sulfides at low P and T. Extremely reducing conditions are produced during serpentinization of peridotite, and could plausibly form metallic PGE phases (Dick, 1974; Dick and Gillete, 1976). The same process has been hypothesized to form FeNi nuggets (Awaruite/Josephenite) found in many ophiolites. Alternatively, the PGA have been hypothesized to form during melting processes (Brenker et al., 2003; Hattori and Cabri,

1992; Okrugin, 2011; Prichard and Lord, 1996; Prichard et al., 2008). In this mechanism, the PGE are primarily hosted in sulfides and sulfide melts. Sulfur is soluble in silicate melts and so is mobilized by melting processes. However, the PGE are largely insoluble in silicate melts and remain in the sulfides, eventually reaching saturation as the sulfide volume decreases. This view is supported by inclusions of refractory olivine and orthopyroxene found in PGA (Brenker et al., 2003; Peck and Keays, 1990; Peck et al., 1992). However, few PGA have been found in-situ in mantle samples (e.g. Prichard et al., 2008), and where they have been found, they are micron sized, much smaller than the detrital grains.

Better constraints on the formation of PGA are important for both economic and scientific reasons. Economically, placer PGA are an important source of PGE (Stribrny et al., 2000). Scientifically, the high concentrations of PGE in PGA grains allow a number of non-traditional isotopic systems to be measured (Bird et al., 1999; Hattori and Cabri, 1992; Luguet et al., 2008; Malitch and Merkle, 2004; Malitch and Thalhammer, 2002; Meibom and Frei, 2002; Meibom et al., 2004; Pearson et al., 2007; Walker et al., 2005). The Re-Os system has been used to evaluate the Os isotopic heterogeneity in the mantle, which constrains mantle mixing efficiency (Luguet et al., 2008; Meibom et al., 2002) and potentially the episodic growth of the continental crust (Pearson et al., 2007). The Pt-Os system has been used to date the formation of layered intrusions and ophiolites (Coggon et al., 2012; Coggon et al., 2011; Nowell et al., 2008). Interestingly, the Pt/Os ratio in individual Pt_3Fe grains has been found to vary during laser-ablation, allowing single grains to be dated by multicollector ICPMS. It is presumed that the variation

during laser-ablation is due to nuggets of varying composition within the PGA grain, but the nature, size and distribution of these nuggets was not determined in the study.

To better understand the formation and chemical composition of PGA, we use laser-assisted atom probe tomography (APT) to image and analyze an isoferroplatinum (Pt_3Fe) PGA grain from northern California. While APT has been used for years on metals in materials science (e.g. Blavette et al., 2008), only the recent development of laser-assisted APT has allowed non-conducting materials to be analyzed (Kelly and Larson, 2012; Seidman, 2007). Thus it is a relatively new method for mineralogy and geoscience and so the process is described in some detail below. Part of the motivation for this study is to evaluate the utility of APT analysis of complex geological materials. Typically APT has been used in materials science on relatively simple materials, typically with fewer than 6 elements, whereas geological materials typically contain 5-10 major elements, and dozens of trace elements. Also, isotopic analyses has not been a focus of material science use of APT, whereas measuring isotopic ratios on ever-smaller volumes is of great geologic interest and a potential major advance offered by APT. For example, Hadean zircons have been analyzed by APT and found to contain trace element clusters (Valley et al., 2014). Further information about APT can be found in these articles (Blavette et al., 2008; Kelly and Larson, 2012; Miller and Forbes, 2009; Miller et al., 2012; Seidman, 2007).

This is a preprint, the final version is subject to change, of the American Mineralogist (MSA)
Cite as Authors (Year) Title. American Mineralogist, in press.
(DOI will not work until issue is live.) DOI: http://dx.doi.org/10.2138/am-2015-4998

ANALYTICAL METHODS

Sample

The sample is a PGA grain from a black sand (chromite) placer deposit in northern California, presumably derived from one of the numerous mantle ophiolite sections found there. The sample was obtained from the Harvard University Mineralogy Museum (specimen 92362). The PGA grain is mostly Os-Ir alloy (osmiridium) with small Pt_3Fe (isoferroplatinum) inclusions (Figure 1). The sample was taken from the Pt_3Fe inclusion.

Sample Preparation

For APT, the sample must be formed into a small needle 1-5 microns in length and 100-200 nm in diameter (Figure 2). For flat samples, this is usually achieved using a dual-beam focused ion beam -scanning electron microscope (FIB-SEM). The sample was first embedded in epoxy and polished to expose the grain. A Ga ion beam (accelerating voltage = 30 kV, current = 9.3 nA) was used to extract a standard lift-out, producing a section roughly 20 μm wide x 7μm deep x 1 μm thick. The end of the section was then attached to a Cu post (with a Pt deposition) and the last 2 microns of the section was cut off with the FIB, leaving a cuboid of the sample attached to the top of the Cu post by Pt. An array of Cu posts was created by cutting a standard TEM grid in half with a razor blade and using the FIB to sharpen the exposed tips. This method of specimen mounting also allows for TEM analysis of the specimens as described in more

detail in Gorman et al. (2008). Typically 6-8 sample needles can be cut from one lift-out. The cuboids are then shaped into needles using lower beam currents (30 kV, 0.43-2.5 nA). At 30 kV, the Ga ions are implanted into the sample 10s of nm. The final step in forming the needle is to 'clean' it using a low accelerating voltage (2.0 kV, 0.72 nA). This limits Ga implantation to the outer 2-5 nm of the needle (Thompson et al., 2007). Final needles are typically 1-5 microns tall with tip radii of 50-100 nm (Figure 2). A detailed description of the sample preparation can be found in Thompson et al. (2007).

Background on APT analysis

Since APT is a new technique for geological sciences, it is worthwhile reviewing its basic operation. During analysis inside the APT device, an annular electrode (local electrode) is positioned near the needle and the specimen highly biased (1000s of volts). The curvature at the tip of needle concentrates the field to extremely high values (10s of V/nm). At high enough voltage, ions are field evaporated from the needle tip and accelerated to a detector plate. Thus the technique is destructive. In traditional APT, the electric field is brought up to just below the evaporation point and then an additional, pulsed bias is applied with the goal of liberating only one ion at a time. This works well for samples with high electrical conductivity, but for non-conductors, the physical stresses produced by the high electric fields usually fractures the needles. More recently, an approach has been developed, in which the electric field is kept constant and at a level just below the evaporation point., then a pulsed, picosecond laser is focused on the needle tip, providing the energy to evaporate ions. The laser pulse rate is typically 100's of kHz. As with the voltage pulsing, ideally each laser pulse liberates a single ion. This requires

lower electrical fields and produces less stress on non-conducting samples. The result is that a wide range of non-conducting materials can now be analyzed with APT, including many geological materials.

The detector in the atom probe is made of a 2D array of channels and so records the location on the detector where the ion hits. Because the ions are only detected if they strike inside the channel the detection efficiency is limited by the open area in the detector (~50-65%). The detected ions can be projected back to the location on the needle tip where the ion originated. Since these are charged particles travelling in an electrostatic environment, the x and y positions are precisely determined from the location of the event on the detector. Atoms detected at the same x-y position are stacked on top of each other in the sequence they were detected. Essentially, a series of atomic layers is formed as the needle is progressively evaporated. These layers are stacked to form a 3D reconstruction of the sample in which the location of each detected ion is known. This provides the possibility of 0.1–0.3 nm spatial resolution in the x-y direction and better than 0.1 nm depth resolution z direction) resolution (Gault et al., 2010). The effective magnification is 1 million times, which is the ratio of the flight path length (90 – 160 mm) to the needle tip radius times the image compression (due to the applied field). In detail, because the tip of the sample needle is curved, atoms evaporated from the center of the needle have a shorter distance to travel to the detector than atoms evaporated from the edges. To account for this in the reconstruction of the atom positions, the sample tip is assumed to be semi-spherical (bowl-shaped). This is called a 'bowl-correction'. The radius of the sample tip is needed to make an accurate reconstruction of the atomic positions but is not measured in the APT analysis. So the

radius must be measured by independent means, usually by TEM imaging of the tip prior to analysis. Because the sample tip is not perfectly spherical, the bowl-correction imparts spherical artifacts into the reconstructions (Figure 3).

Because the specimens are tapered, as material is evaporated, the tip becomes progressively duller (larger tip radius). The increasing sample radius requires the field voltage to be continually increased to maintain a constant field on the tip surface and so maintain a constant evaporation-rate (typically 1000s to 10,000s of atoms per second). At some point, the voltage increases to the point at which the sample or sample attachment to the post fails by the physical stresses imparted by the field. The failure can be surprisingly violent, leaving little or none of the specimen, and so analyses are ideally stopped prior to tip failure, which allows for post APT analysis TEM imaging. This information assists in generating more accurate reconstructions. Typically 1-10 million atoms are detected in each run, representing 100,000 cubic nm of material (Figure 2), though much longer runs (up to 1 billion ions) have been performed, depending on the material and specimen geometry.

The detector also records the time of the ion detection with a resolution of 50 ps. Assuming the ion was released at the time of the laser (or voltage) pulse, the time-of-flight can be measured for each ion. Because the applied bias and distance from the tip to the detector is known, the mass to charge ratio (m/q) of each detected ion can be calculated. Thus the atom probe is also a time-of-flight (TOF) mass spectrometer.

The end product of APT analysis is the position of each detected ion in 3 dimensions and its m/q ratio. This information can be used to produce a 3D reconstruction of the atoms in the analyzed volume and can be post-processed to extract a

wide range of information, from the elemental and isotopic composition of nm-scale inclusions, to the crystal structure of the material. This combination of angstrom spatial resolution and ppm level detection limits is unique and potentially of great use to geochemical studies. Several review articles on atom probe provide further information about the methods and its applications (Blavette et al., 2008; Kelly and Larson, 2012; Miller and Forbes, 2009; Seidman, 2007)

Analytical Procedure

Five sample tips were analyzed (online Table 1) using the CAMECA LEAP 4000 XSi at the Colorado Center for Advanced Ceramics at the Colorado School of Mines. Images for only one (747) are shown below. The laser energy used was 120 to 275 pJ. The laser pulse rate was 500 kHz. The ion detection rate was set at 1 to 3 ions per pulse and maintained by the software by steadily increasing the voltage. The analysis was stopped after 10 million ions were detected. The total volume evaporated was 50 nm high and 50 nm in diameter (~100,000 nm^3, Figure 2).

The shape of the needle was reconstructed using a 60 nm tip radius and a constant shank angle of 15° (Figure 3). The reconstruction parameters were selected to produce flat atomic planes with an interplanar spacing that matched that of isoferroplatinum: 0.223 nm between (111) planes.

Time-of-flight analysis

Mass-charge histograms are shown in Figure 4. Background counts are very low, typically <10 counts across the entire range with a standard deviation of <1. Using 5 SD above background as the detection limits, peaks as low as 10 counts are detectible. For 10 million atoms detected, that translates into theoretical single-peak detection limits of ~1 ppm atomic. Peaks for individual ions are largely symmetrical. The Fe^{2+} peaks (at m/q<30) are slightly skewed to higher m/q. The skewness (termed 'thermal tails') is due to the sample being over-heated by the laser to the point that ions are released at some time after the laser pulse, contrary to the base assumption. These late-evaporating ions reach the detector later and so are assigned artificially long times-of-flight, skewing the peaks to higher m/q. The vast majority of atoms were detected as single ions. For Pt, Ir, Rh, Fe and Ni singly and doubly charged ions are sub-equal in concentration, with the doubly charged ions being slightly more abundant. Ru and Co are predominantly 2+. Cu is predominantly single charged. These variations result from the differences in the fields necessary for single and multiple ionization of the different species (Tsong, 1978).

The only molecular species detected were $^{196}PtH^{+}$ and $^{198}PtH^{+}$ (Figure 4). Hydride generation varies from 0.3 to 1.8 % relative (average of 1% for four samples analyzed) for these ions. For the sample analysis given in the tables and shown in the figures, hydride generation was 0.4% relative. Presumably $^{192}PtH^{+}$, $^{194}PtH^{+}$ and $^{195}PtH^{+}$ were also formed but are not detected because of m/q peak overlaps with ^{193}Ir, ^{195}Pt and ^{196} Pt. No doubly charged PtH^{2+} was detected. After background correction, the composition of the needle was determined simply by counting the number of detected ions (online Table 1). No calibration is used, implicitly assuming that mass fractionation is negligible. All ions in a given m/q band (gray bands in figure 4) are attributed to a

single ion. No corrections for peak overlaps were made. Because the majority of the PtH peak interferences are with Pt peaks, the effect on the estimated Pt concentrations is minimal. Only the Pt associated with $^{192}PtH^{+}$ cannot be counted. For individual Pt isotopes, the $^{192}Pt^{+}$,$^{194}Pt^{+}$ and $^{198}Pt^{+}$ should be 0.4% relative low due to hydride formation, which is within error of the analyses. The peak at $^{195}Pt^{+}$ should be affected by formation (loss) of $^{195}PtH^{+}$, but this should be roughly counterbalanced by formation (gain) of $^{194}PtH^{+}$ since ^{194}Pt has a similar abundance to ^{195}Pt. The same is true for the $^{196}Pt^{+}$ peak. All ions at m/q 193 are assigned to ^{193}Ir. The Ga peaks are attributed to contamination from the FIB Ga beam used to shape the needle and are not included in the analysis. The concentration of these species around only the edges of the specimen support this assumption.

EMPA and EBSD

To confirm the chemical and structural results of the APT analysis, the PGA grain has been analyzed by electron microprobe analysis (EMPA) and electron backscattered diffraction (EBSD) at Brown University. EMPA was performed on a CAMECA SX 100 Electron Microprobe, using a focused beam. For Pt, Fe, Ir, Ni, Rh, Ru and Co, an accelerating voltage of 20kV was used and a beam current of 20nA. The surrounding Os grain produced a fluorescence that overlaps Cu, and so Cu was analyzed using a 5 kV beam on the Lα peak. No other fluorescence peaks were detected. Counting times were 45s for each element. EMPA data are given in online Table 2.

EBSD was performed with a JEOL 845 SEM at 20kV and a probe current of 6nA. The sample was polished with colloidal silica and carbon coated. A total of 16 points

were analyzed. The data were processed with Oxford/HKL Technology's Channel 5 software. The pole figures are contoured with a halfwidth of 15^{o} and a global maximum of 16.8 times above global maximum (Figure 5).

RESULTS

Elemental composition

The elemental composition of the grain is given in Table 1 and shown in Figure 6. Except Rh, all APT values are within 1 standard deviation of the EMPA data (Table 1). The composition of the grain is typical for ophiolite-related isoferroplatinum with 78.94 wt% Pt and 9.66 wt% Fe (Cabri et al., 1996; Ford, 1981; Malitch and Thalhammer, 2002; Tolstykh et al., 2009). Co is the lowest concentration element detected at 110 +/-20 ppm.

The origin of the low APT values relative to the EMPA data for Rh is not clear. One possibility is that molecular species (hydrides or dimers) were formed, which were not identified and so not included in the composition. However, no dimers of any element were detected. Based up the PtH peaks (Figure 4), hydride generation is about 5%. Both the Rh^{+} and Rh^{2+} m/q peaks are well resolved and symmetric (Figure 4). Alternatively, there could be real sub-micron compositional variations that are detectable by APT, but below the spatial resolution of EMPA.

Isotopic composition

The isotopic composition, as determined by APT, is given in Table 2 and shown in Figure 7. The isotope ratios agree well with NIST values (Bohlke et al., 2005). While

these are not direct measurement of the sample, the variation in the isotope ratios is much smaller than the analytical error of the APT analyses. Of the 25 ratios measures, 20 are within 5% relative of the NIST values, with 4 of the 5 values outside of 5% being at concentrations below 0.1 wt %.

Spatial Resolution

Near the center of the reconstruction, there is a crystallographic pole (Figure 5). Here the trajectory aberrations and out of sequence evaporation are least, and, therefore, the positions of the atoms are most accurately resolved. The atoms lie along parallel planes which we interpret to be the atomic planes of the isoferroplatinum structure (Figure 4). This is not a reconstruction artifact and has been seen in reconstructions of other metals including Al (Gault et al, 2010) and W (Kelly et al., 2007). Which atomic planes in the Pt_3Fe structure the aligned atoms represent can be determined by looking at a histogram of events on the detector (Figure 5a). This displays a clear hexagonal-like symmetry. For an isotropic material, the histogram should be featureless, with the same numbers of detections at all positions on the detector. The lines (areas of lower detection) in the histogram are produced because of differences in bond strength and local potential for different crystal faces. These differences result in local electrical field variations and trajectory aberrations, such that there is a reduction of ion detections along zone lines. The effect is most pronounced at poles (where zone lines meet) Note the variation in detected events in Figure 5a. Isoferroplatinum is face-centered cubic (fcc) in the disordered form and so displays hexagonal-like symmetry (three-fold rotation axis) only on the (111) plane. The hexagonal symmetry of the lines in Figure 5a imply

that the image is looking down the <111> direction, which is tilted from horizontal by ~5 degrees. This is confirmed by EBSD analysis of the PGA grain (Figure 5b). The spacing between the (111) planes in isoferroplatinum is 0.223 nm. A histogram of atom positions in the Z direction (Figure 8b) shows peaks where the atomic planes are. The distance between the peaks has been set to 0.223 nm by adjusting the reconstruction parameters. The width of the peaks in Figure 8b suggests a spatial precision of +/- 0.05 nm (peak width at half of maximum peak height). Note that there are places in the reconstruction where the spacing appears larger (Figure 3 inset) than in the bulk of the sample. These are artifacts that occur when the laser power is changed during the analysis and the voltage adjusts. They appear curved in the reconstruction (Figure 3) because of the curved shape of the needle tip.

Distribution of minor elements

A unique feature of APT is that it can determine the location of minor and trace elements with nm-scale precision. Figure 8a shows the position minor/trace elements (larger circles) in the central portion of the sample. As with the Pt and Fe atoms (small dots), the minor elements fall along atomic planes. Notably, there are small areas 1-2 nm in size that appear free from all elements other than Pt and Fe (Figure 8a, dashed line). The atomic planes are still apparent in the Pt and Fe atoms, so it seems unlikely that the minor element free regions are an artifact of the evaporation, or else it would have disrupted the imaging of the planes. Directional migration on the surface of the sample tip can produce variations in the apparent distribution of solute elements (Gault et al., 2012). However, the migration decreased to negligible levels at the low temperatures

(40K) and laser energies (pJ) used in this study. Moreover, the amount of migration was different for different atoms depending upon their polarizability (Gault et al., 2012). Thus the completely minor element free regions are hard to explain as due to migration.

One possible explanation for the pure Pt-Fe regions is that they are simply the result of a random distribution of atoms, which is different than an even distribution. This can be tested by measuring the distribution of nearest neighbor distances and comparing it to a calculated random distribution (Figure 9). In this case, the distance is the distance from a minor element to the nearest minor element. That is, Pt and Fe are not included, as we are interested in determining the distribution of minor elements. Compared to a random distribution, a clumped distribution will have a peak at shorter inter-atomic distances, while a more even distribution will have a distribution peak at a larger distance. For the PGA grain, the observed peak in the nearest neighbor distribution is shifted ~0.02nm shorter than that of a random distribution (Figure 9). This difference is smaller than the spatial resolution of the atom probe and so is not considered statistically significant, suggesting that the minor elements are randomly distributed.

If so, this has some interesting implications. For one, such 'pure' regions will have different parent-daughter ratios (e.g. Pt/Os) than the bulk of the crystal, and so could potentially be used to produce a two mineral isochron from a single crystal, as if they were essentially two different minerals. While the individual, nm-scale 'pure' regions contain too few atoms (10-100's) for this to be done accurately, using the 3D spatial resolution of the APT image, the 'pure' regions could be isolated and averaged together. This would only be appropriate if the pure regions were all formed at the same time. For the ^{190}Pt-^{186}Os system, with a half-life of 3.7×10^{11} yrs (Tavares et al, 2006), and assuming

a conservative quantification limit of 100 ppm, this would require roughly 2 billion atoms of Pt with standard isotope ratios to produce enough ^{186}Os in ~170 million years (the age of the California ophiolites) to be dateable. This is much larger than our standard analyses (10 million atoms), but over a billion atoms have been imaged in single runs of synthesized metal wires. So it may be feasible in the near future to do this, for example, by analyzing 200 million atoms in 10 separate needles of the same sample. The other challenge is isolating the pure regions. This is non-trivial using existing software, which have been designed to isolate high-concentration areas, not low concentration areas. Second, the concentration of minor and trace elements into the 'matrix' material, may alter its chemical properties (e.g. diffusivity, solubility of volatiles...) and physical properties (e.g. bulk and shear modulus, electrical conductivity, magnetic susceptibility...). One avenue of future research is to correlate the 3D distribution of minor and trace elements with the chemical and physical properties.

Order-disorder precipitates

Alternatively, the areas may not be random, but may be order-disorder precipitates, similar to those seen in synthetic metal alloys (Radmilovic et al., 2011; Srinivasan et al., 2009). At high temperatures, the atomic composition Pt_3Fe is face-centered cubic with a disordered distribution of Pt and Fe - part of a complete solid solution between the end-member metals (e.g. Nose et al., 2003). At ambient pressures and temperatures below ~1600K, at equilibrium the Pt and Fe become ordered and the structure becomes simple cubic, specifically the $L1_2$ structure (in the *Strukturbericht* designation; e.g. Kelly and Groves, 1970) - an atomic basis of Fe at (0,0,0) (i.e. the unit

cell corner) and Pt at (½,½,0), (½,0,½) and (0,½,½) (the unit cell faces). Similar systems (Cu_3Au, AlLiSc) have been studied in which the ordered phase precipitates from the fcc phase. The precipitates are nm in scale and can expel trace elements (core-shell precipitates; Radmilovic *et al.*, 2011). Many of the minor element free regions are disc shaped and oriented at 45° to the (111) atomic planes, consistent with exsolution (Figure 8a). In sum, the precipitates seen in synthetic systems are similar in many respects to the nm-scale pure regions we have observed in the natural Pt_3Fe.

The next question is whether it is energetically reasonable that formation of the ordered Pt_3Fe phase could expel minor and trace elements. The thermodynamics of the trace-element expulsion associated with the formation of the ordered, $L1_2$-structure Pt_3Fe precipitates can be comprehended by reference to the solution models (Fredriksson and Sundman, 2001). That the high-temperature fcc solid solution would form an ordered compound as temperature is lowered is indicative of an exothermic solution, i.e., the activity coefficients for Fe and Pt being distinctly less than unity. This is indeed the case: for the composition 75 at% Pt, 25 at% Fe, the (metastable) Gibbs excess calculated for T = 300K is $G^{E,fcc} \cong -44.3$ kJ mol^{-1} while that for the ideal solution is $G^{id,fcc} \cong -1.4$ kJ mol^{-1}. Neither value is anticipated to change greatly by solution substitution of Ir for Pt and of Ni + Co + Cu for Fe as the degrees of substitution are modest (cf. Table 1). The sum of $G^{E,fcc} + G^{id,fcc}$ ($\cong -45.7$ kJ mol^{-1}) can be compared to that for $G^{L1_2,Pt_3Fe} \cong -49.9$ kJ mol^{-1}; the difference in Gibbs energies exceeds significantly the absolute value of G^{id}; it is handily large enough to overcome the entropy of solution and so could purge impurities from the $L1_2$-ordered precipitates. Thus we conclude that formation of trace element-free regions by order-disorder precipitates is energetically possible.

If the pure Pt-Fe areas are ordered precipitates, it lends support to the high-temperature formation model for the grains because the precipitates only form at igneous temperatures. If the grains were formed at low, hydrothermal temperatures (<500^{o}C), then the entire grain should be ordered (Nose et al., 2003). EBSD analysis indicates that the grain is largely fcc, strongly supporting a high temperature origin. The inclusions are too small to be analyzed by EBSD and so their structure was not determined directly. Potentially, TEM could be used to determine their structure.

IMPLICATIONS

Our study has implications for both the study of platinum group alloys and for the future of analytical geochemistry. For PGA formation, the APT analyses may support an igneous origin for such grains. Nanometer-scale regions free of trace and minor elements may be order-disorder precipitates, which could only have formed if the PGA grain cooled from magmatic temperatures. For analytical geochemistry, APT is a step closer to an ultimate chemical analysis, in which the isotopic identity and position of every atom in a material are known. APT is increasingly common in materials science, but typically is used on simpler materials with fewer than 6 elements. Geochemical studies, on the other hand, are typically concerned with complex materials with a dozen major/minor elements and numerous trace elements. Also, precise analysis of isotopic ratios is of wide interest in geoscience. This study demonstrates that APT can provide accurate analysis of both elemental and isotopic compositions on complex, natural materials. The history of geochemistry is that major advances in analytical capabilities (e.g. electron microprobe, transmission electron microscopy, secondary ion mass spectrometry, laser-ablation

ICMPS) spawn new fields of geoscience (e.g. melt inclusion studies, dating of individual zircons, ...) and drive much of the growth in the field. APT may well be the next such fundamental leap in analytical capability. One note of caution to moderate such enthusiasm, the current study is to some extent a best-case scenario. Metals are ideal materials for APT as they are electrical conductors and contain only metallic bonds. Silicates, with covalent Si-O bonds and limited electrical conductivity present a much bigger analytical challenge, one which is actively being addressed.

Acknowledgements

We thank Rita Kirchhofer for her assistance with FIB sample preparation and APT analysis. Amanda Goetsinger is thanked for assistance with the EBSD analyses and Joe Boesenberg for his assistance with the EMPA analyses. This research was supported by a Salomon Grant from Brown University and NSF grant EAR1144668. The atom probe instrument used was funded by NSF Award Number 1040456.

References

Bird, J.M., and Bassett, W.A. (1980) Evidence of a deep mantle history in terrestrial osmium-iridium-ruthenium alloys. Journal of Geophysical Research, 85(NB10), 5461-5470.

Bird, J.M., Meibom, A., Frei, R., and Nagler, T.F. (1999) Osmium and lead isotopes of rare OsIrRu minerals: derivation from the core-mantle boundary region? Earth And Planetary Science Letters, 170(1-2), 83-92.

Blavette, D., Al Kassab, T., Cadel, E., Mackel, A., Vurpillot, F., Gilbert, M., Cojocaru, O., and Deconihout, B. (2008) Laser-assisted atom probe tomography and nanosciences. International Journal of Materials Research, 99(5), 454-460.

Bohlke, J.K., de Laeter, J.R., De Bievre, P., Hidaka, H., Peiser, H.S., Rosman, K.J.R., and Taylor, P.D.P. (2005) Isotopic compositions of the elements, 2001. Journal of Physical and Chemical Reference Data, 34(1), 57-67.

Brenker, F.E., Meibom, A., and Frei, R. (2003) On the formation of peridotite-derived Os-rich PGE alloys. American Mineralogist, 88(11-12), 1731-1740.

Cabri, L.J., Harris, D.C., and Weiser, T.W. (1996) Mineralogy and distribution of platinum-group mineral (PGM) placer deposits of the world. Exploration and Mining Geology, 5(2), 73-167.

Coggon, J.A., Nowell, G.M., Pearson, D.G., Oberthuer, T., Lorand, J.P., Melcher, F., and Parman, S.W. (2012) The Pt-190-Os-186 decay system applied to dating platinum-group element mineralization of the Bushveld Complex, South Africa. Chemical Geology, 302, 48-60.

Coggon, J.A., Nowell, G.M., Pearson, D.G., and Parman, S.W. (2011) Application of the pt-190-os-186 isotope system to dating platinum mineralization and ophiolite

formation: an example from the Meratus Mountains, Borneo. Economic Geology, 106(1), 93-117.

Dick, H.J.B. (1974) Terrestrial nickel-iron from Josephine peridotite, its geologic occurrence, associations, and origin. Earth And Planetary Science Letters, 24(2), 291-298.

Dick, H.J.B., and Gillete, H. (1976) Josephinite - specimens from Earths core - discussion. Earth And Planetary Science Letters, 31(2), 308-311.

Ford, R.J. (1981) Platinum-Group Minerals In Tasmania. Economic Geology, 76(2), 498-504.

Fredriksson, P. and Sundman, B. (2001) A thermodynamic assessment of the Fe-Pt system. Calphad–Computer Coupling of Phase Diagrams and Thermochemistry, 25(4), 535-548.

Gault, B., Danoix, F., Hoummada, K., Mangelinck, D., and Leitner, H. (2012) Impact of directional walk on atom probe microanalysis. Ultramicroscopy, 113, 182-191.

Gault, B., Moody, M.P., De Geuser, F., La Fontaine, A., Stephenson, L.T., Haley, D., and Ringer, S.P. (2010) Spatial resolution in atom probe tomography. Microscopy and Microanalysis, 16(1), 99-110.

Gorman, B., Diercks, D., Salmon, N., Stach, E., Amador, G., and Hartfield, C. (2008) Hardware and techniques for cross-correlative TEM and atom probe analysis. Microsc. Today, 16(4), 42-47.

Harris, D.C., and Cabri, L.J. (1991) Nomenclature of platinum-group-element alloys - review and revision. Canadian Mineralogist, 29, 231-237.

Hattori, K., and Cabri, L.J. (1992) Origin Of Platinum-Group-Mineral Nuggets Inferred From An Osmium-Isotope Study. Canadian Mineralogist, 30, 289-301.

Kelly, T.F., Geiser, B.P., and Larson, D.J. (2007) Definition of spatial resolution in atom probe tomography. Microscopy and Microanalysis, 13(S02), 1604-1605.

Kelly, T.F., and Larson, D.J. (2012) Atom probe tomography 2012. Annual Review of Materials Research, Vol 42, 42, 1-31.

Luguet, A., Pearson, D.G., Nowell, G.M., Dreher, S.T., Coggon, J.A., Spetsius, Z.V., and Parman, S.W. (2008) Enriched Pt-Re-Os isotope systematics in plume lavas explained by metasomatic sulfides. Science, 319(5862), 453-456.

Malitch, K.N., and Merkle, R.K.W. (2004) Ru-Os-Ir-Pt alloys from the Evander Goldfield (Witwatersrand Basin, South Africa): osmium isotope evidence for the oldest PGE-mineralization on Earth. Geochimica Et Cosmochimica Acta, 68(11), A772.

Malitch, K.N., and Thalhammer, O.A.R. (2002) Pt-Fe nuggets derived from clinopyroxenite-dunite massifs, Russia: A structural, compositional and osmium-isotope study. Canadian Mineralogist, 40, 395-418.

Meibom, A., and Frei, R. (2002) Evidence for an ancient osmium isotopic reservoir in Earth. Science, 296(5567), 516-518.

Meibom, A., Frei, R., and Sleep, N.H. (2004) Osmium isotopic compositions of Os-rich platinum group element alloys from the Klamath and Siskiyou Mountains. Journal Of Geophysical Research-Solid Earth, 109(B2) doi:10.1029/2003JB002602.

Meibom, A., Sleep, N.H., Chamberlain, C.P., Coleman, R.G., Frei, R., Hren, M.T., and Wooden, J.L. (2002) Re-Os isotopic evidence for long-lived heterogeneity and equilibration processes in the Earth's upper mantle. Nature, 419(6908), 705-708.

Miller, M.K., and Forbes, R.G. (2009) Atom probe tomography. Materials Characterization, 60(6), 461-469.

Miller, M.K., Kelly, T.F., Rajan, K., and Ringer, S.P. (2012) The future of atom probe tomography. Materials Today, 15(4), 158-165.

Nowell, G.M., Coggon, J.A., Pearson, D.G., Parman, S.W., Hanski, E., and Tuisku, P. (2008) Precise and accurate $^{186}Os/^{188}Os$ and $^{187}Os/^{188}Os$ measurements by multi-collector plasma ionisation mass Spectrometry, part II: laser ablation and its application to single-grain Pt–Os and Re–Os geochronology. Chemical Geology 248, 394-426.

Okrugin, A.V. (2011) Origin of platinum-group minerals in mafic and ultramafic rocks: from dispersed elements to nuggets. Canadian Mineralogist, 49(6), 1397-1412.

Pearson, D.G., Parman, S.W., and Nowell, G.M. (2007) Osmium isotopes show a link between mantle melting events and crustal growth. Nature, in review.

Peck, D.C., and Keays, R.R. (1990) Insights into the behavior of precious metals in primitive, S-undersaturated magmas - evidence from the Heazlewood River Complex, Tasmania. Canadian Mineralogist, 28, 553-577.

Peck, D.C., Keays, R.R., and Ford, R.J. (1992) Direct crystallization of refractory platinum-group element alloys from boninitic magmas - evidence from western Tasmania. Australian Journal Of Earth Sciences, 39(3), 373-387.

Prichard, H.M., and Lord, R.A. (1996) A model to explain the occurrence of platinum- and palladium-rich ophiolite complexes. Journal of the Geological Society, 153, 323-328.

Prichard, H.M., Neary, C.R., Fisher, P.C., and O'Hara, M.J. (2008) PGE-rich podiform chromitites in the Al 'Ays ophiolite complex, Saudi Arabia: an example of critical mantle melting to extract and concentrate PGE. Economic Geology, 103(7), 1507-1529.

Seidman, D.N. (2007) Three-dimensional atom-probe tomography: Advances and applications. Annual Review of Materials Research, 37, p. 127-158.

Stribrny, B., Wellmer, F.W., Burgath, K.P., Oberthur, T., Tarkian, M., and Pfeiffer, T. (2000) Unconventional PGE occurrences and PGE mineralization in the Great

Dyke: metallogenic and economic aspects. Mineralium Deposita, 35(2-3), 260-281.

Tavares, O.A.P, Terranova, M.L., and Medeiros E.L. New evaluation of alpha decay half-life of ^{190}Pt isotope for the Pt-Os dating system. Nuclear Instruments and Methods in Physics Reserach B, 243, 256-260.

Thompson, K., Lawrence, D., Larson, D.J., Olson, J.D., Kelly, T.F., and Gorman, B. (2007) In situ site-specific specimen preparation for atom probe tomography. Ultramicroscopy, 107(2-3), 131-139.

Tolstykh, N., Sidorov, E., and Kozlov, A. (2009) Platinum-group minerals from the Olkhovaya-1 placers related to the Karaginsky ophiolite complex, Kamchatskiy Mys peninsula, Russia. Canadian Mineralogist, 47(5), 1057-1074.

Tsong, T.T. (1978) Field-Ion Image-Formation. Surface Science, 70(1), 211-233.

Valley, J.W., Cavosie, A.J., Ushikubo, T., Reinhard, D.A., Lawrence, D.F., Larson, D.J., Clifton, P.H., Kelly, T.F., Wilde, S.A., Moser, D.E., and Spicuzza, M.J. (2014) Hadean age for a post-magma-ocean zircon confirmed by atom-probe tomography. Nature Geoscience, 7(3), 219-223.

Walker, R.J., Brandon, A.D., Bird, J.M., Piccoli, P.M., McDonough, W.F., and Ash, R.D. (2005) Os-187-Os-186 systematics of Os-Ir-Ru alloy grains from southwestern Oregon. Earth And Planetary Science Letters, 230(1-2), 211-226.

Figure Captions

Figure 1. Pt_3Fe (darker gray) inclusions in osmiridium grain (lighter gray). The black square consuming bottom left edge of Pt_3Fe inclusion is FIB pit.

Figure 2. Pt_3Fe sample needle shaped with FIB. The small white box is the projection of the volume imaged by APT (~50 nm on a side). The upper left image shows all 10 million atoms detected in perspective view.

Figure 3. Pt and Fe atoms in slice through alloy grain. The slice is ~50 nm tall and 5 nm thick. The black dots are Pt and Fe atoms which constitute 88 mole% of the sample. The arcuate lines (highlighted by dashed line) in the reconstruction are an artifact of the bowl correction (see text for further discussion). Thin black line outlines volume where the imaging artifacts are minimized and atomic planes are resolvable (inset).

Figure 4. Mass/charge (m/q) spectra. Background for all peaks is less than ten for the entire run (10 million counts, note log scale on y-axis). The symmetry of the peaks suggests there is little heating of the sample, which would produce asymmetric peaks skewed to higher m/q values (thermal tails). A small amount of $^{198}PtH+$ is detectable and is included in the Pt concentrations.

Figure 5. a) Histogram of number of atoms striking each pixel of the APT detector (darker = more detections). The hexagonally arranged white lines are low detection areas related to the crystal symmetry of the isoferroplatinum (hexagonal on the (111) plane). The white dot near the center is the {111} pole, which is 5^o to the left of vertical. b) EBSD {111} pole figure showing {111} pole with the same 5^o offset as in the histogram.

Figure 6. Elemental composition determined by APT compared to EMPA analysis. Error bars are 1 sigma standard deviation on 12 EMPA analyses. Cu was corrected for x-ray

fluorescence from Os in the surrounding grain (see text). Values given in Table 1 and online Table 1.

Figure 7. APT isotope analysis compared to published NIST values. a) atomic fraction of isotope (counts isotope/total counts element) determined by APT compared to values from NIST (Bohlke et al, 2005). b) % difference between APT and NIST isotope fractions versus atomic concentration of isotope. The majority of isotope fractions are within 5% of the NIST values. Values given in Table 2 and online Table 2.

Figure 8. A) Locations of atoms: small dots are Pt and Fe, larger dots are minor elements (Ir, Ru, Rh, Cu, Ni, Co). Lattice planes (black lines) are 0.223 nm apart. The dashed ellipse outlines a region of Pt-Fe that apparently is free of any other elements. Numerous of these minor and trace element-free regions are seen throughout the sample. B) Histogram of distances between atoms in the Z direction. Peak at 0.223 nm is the [111] lattice plane spacing.

Figure 9. Nearest neighbor distribution between minor elements (Ir, Ru, Rh, Cu, Ni, Co). Gray line is observed distribution. Dashed line is a calculated random distribution. The similarity indicates there is no apparent clustering of atoms.

This is a preprint, the final version is subject to change, of the American Mineralogist (MSA)
Cite as Authors (Year) Title. American Mineralogist, in press.
(DOI will not work until issue is live.) DOI: http://dx.doi.org/10.2138/am-2015-4998

Table 1. Comparison of electron microprobe and APT analysis of element concentrations

	EMPA (n=5)*	stdev	APT (n=5)*	stdev
Pt	79.4	0.2	78.9	0.7
Fe	9.4	0.1	9.7	0.4
Ir	8.6	0.2	8.9	0.9
Ni	1.03	0.03	1.03	0.04
Cu	0.48	0.02	0.51	0.04
Rh	1.00	0.01	0.82	0.03
Ru	0.12	0.02	0.14	0.06
Co	0.018	0.005	0.011	0.002
Sum	100.00		100.00	

* values in wt%

This is a preprint, the final version is subject to change, of the American Mineralogist (MSA)
Cite as Authors (Year) Title. American Mineralogist, in press.
(DOI will not work until issue is live.) DOI: http://dx.doi.org/10.2138/am-2015-4998

Table 2. Comparison of isotope analysis by APT with published NIST values

element	isotope	fraction (NIST)*	error*	fraction (APT)**	percent difference	isotope concentration (atomic %)
Pt	190	0.00014	0.00001	0.00016	11.9	0.010
	192	0.00782	0.00007	0.00856	8.61	0.52
	194	0.32967	0.00099	0.32052	-2.86	19.5
	195	0.33832	0.0001	0.33762	-0.21	20.5
	196	0.25242	0.00041	0.26036	3.05	15.8
	198	0.07163	0.00055	0.07279	1.59	4.42
Fe	54	0.05845	0.00035	0.05846	0.01	1.54
	56	0.91754	0.00036	0.91928	0.19	24.3
	57	0.02119	0.0001	0.02226	4.82	0.588
	58	0.00282	0.0004	Ni interference		
Ir	191	0.373	0.002	0.369	-1.05	2.69
	193	0.627	0.002	0.631	0.61	4.61
Ni	58	0.680769	0.000089	0.687111	0.92	1.86
	60	0.262231	0.000077	0.254064	-3.21	0.686
	61	0.011399	0.00006	0.011963	4.71	0.032
	62	0.036345	0.000017	0.036124	-0.61	0.098
	64	0.009256	0.000009	0.010738	13.8	0.029
Cu	63	0.6915	0.0015	0.6892	-0.34	0.896
	65	0.3085	0.0015	0.3108	0.75	0.404
Ru	96	0.0554	0.0014	0.0577	3.93	0.017
	98	0.0187	0.0003	0.0177	-5.56	0.005
	99	0.1276	0.0014	0.1300	1.81	0.039
	100	0.1260	0.0007	0.1228	-2.64	0.037
	101	0.1706	0.0002	0.1658	-2.87	0.050
	102	0.3155	0.0014	0.3097	-1.87	0.093
	104	0.1862	0.0027	0.1964	5.18	0.059

* values from Bohlke et al (2005)
** values from analysis 747

This is a preprint, the final version is subject to change, of the American Mineralogist (MSA)
Cite as Authors (Year) Title. American Mineralogist, in press.
(DOI will not work until issue is live.) DOI: http://dx.doi.org/10.2138/am-2015-4998

online Table 1. Individual electron microprobe analyses

EMPA analyses

	1*	2	3	4	5
Pt	77.40	77.67	77.78	78.27	78.84
Fe	9.23	9.20	9.10	9.08	9.41
Ir	8.60	8.64	8.46	8.26	8.26
Rh	0.98	0.96	0.95	1.03	0.97
Cu	0.45	0.49	0.47	0.47	0.49
Ni	1.00	1.01	1.01	0.99	1.03
Ru	0.13	0.11	0.11	0.13	0.09
Co	0.02	0.02	0.01	0.02	0.02
Total	97.81	98.10	97.89	98.25	99.11

normalized values

	1	2	3	4	5	average	stdev
Pt	79.13	79.17	79.46	79.67	79.55	79.4	0.2
Fe	9.44	9.38	9.30	9.24	9.49	9.4	0.1
Ir	8.79	8.81	8.64	8.41	8.33	8.6	0.2
Rh	1.00	0.98	0.97	1.05	0.98	1.00	0.03
Cu	0.46	0.50	0.48	0.48	0.50	0.48	0.02
Ni	1.02	1.03	1.03	1.01	1.04	1.03	0.01
Ru	0.13	0.11	0.11	0.13	0.09	0.12	0.02
Co	0.02	0.02	0.01	0.02	0.02	0.018	0.005
Total	100.00	100.00	100.00	100.00	100.00	100.00	

* values in wt%

online Table 2. Individual APT analyses

		Uncorrected			Background Corrected			
Sample	**Ion Type**	**Ion Count**	**Ionic Fraction**	**Ionic Fraction (sigma)**	**Background Count**	**Ion Count**	**Ionic Fraction**	**Ionic Fraction (sigma)**
743	Fe	318433	0.263538	5.25E-04	1899	316534	0.264398	5.28E-04
	Pt	730428	0.604508	8.96E-04	3829	726599	0.606922	9.03E-04
	Ir	89050	0.073698	2.56E-04	1183	87867	0.073394	2.57E-04
	Au	211	0.000175	1.20E-05	223	-12	0.000000	0
	Rh	15454	0.012790	1.04E-04	502	14952	0.012489	1.03E-04
	Ru	4505	0.003728	5.57E-05	804	3701	0.003091	5.09E-05
	Ni	33648	0.027847	1.54E-04	1588	32060	0.026779	1.52E-04
	Cu	15653	0.012955	1.04E-04	663	14990	0.012521	1.03E-04
	Ga	318	0.000263	1.48E-05	229	89	0.000075	7.90E-06
	Co	602	0.000498	2.03E-05	207	395	0.000330	1.66E-05
745	Fe	981956	0.257431	2.91E-04	2012	979944	0.257724	2.92E-04
	Pt	2251747	0.590321	4.96E-04	3186	2248561	0.591368	4.97E-04
	Ir	296047	0.077612	1.48E-04	996	295051	0.077598	1.48E-04
	Au	41299	0.010827	5.36E-05	236	41063	0.010799	5.36E-05
	Rh	47753	0.012519	5.76E-05	532	47221	0.012419	5.75E-05
	Ru	10306	0.002702	2.67E-05	852	9454	0.002486	2.56E-05
	Ni	100666	0.026391	8.43E-05	1826	98840	0.025995	8.38E-05
	Cu	45137	0.011833	5.60E-05	902	44235	0.011634	5.56E-05
	Ga	14713	0.003857	3.19E-05	242	14471	0.003806	3.17E-05
	Co	1376	0.000361	9.73E-06	219	1157	0.000304	8.95E-06
	Os	23446	0.006147	4.03E-05	1139	22307	0.005867	3.94E-05
746	Fe	2212305	0.267396	2.02E-04	3191	2209114	0.267574	2.03E-04
	Pt	5002586	0.604650	3.42E-04	5054	4997532	0.605316	3.43E-04
	Ir	517970	0.062606	8.97E-05	1580	516390	0.062547	8.97E-05
	Au	61009	0.007374	3.00E-05	375	60634	0.007344	2.99E-05
	Rh	96981	0.011722	3.79E-05	844	96137	0.011644	3.78E-05

online Table 2. (continued)

		Uncorrected				Background Corrected		
Sample	**Ion Type**	**Ion Count**	**Ionic Fraction**	**Ionic Fraction (sigma)**	**Background Count**	**Ion Count**	**Ionic Fraction**	**Ionic Fraction (sigma)**
746 (cont.)	Ru	11890	0.001437	1.32E-05	1351	10539	0.001277	1.24E-05
	Ni	229042	0.027684	5.86E-05	2897	226145	0.027391	5.84E-05
	Cu	110512	0.013357	4.04E-05	1431	109081	0.013212	4.03E-05
	Ga	28676	0.003466	2.05E-05	384	28292	0.003427	2.04E-05
	Co	2554	0.000309	6.11E-06	347	2207	0.000267	5.69E-06
747	Fe	2281319	0.270327	2.02E-04	2167	2279152	0.270450	2.02E-04
	Pt	5159102	0.611333	3.42E-04	3433	5155669	0.611785	3.42E-04
	Ir	527172	0.062468	8.87E-05	1073	526099	0.062428	8.87E-05
	Au	22908	0.002715	1.80E-05	255	22653	0.002688	1.79E-05
	Rh	99380	0.011776	3.76E-05	573	98807	0.011725	3.75E-05
	Ru	8951	0.001061	1.12E-05	918	8033	0.000953	1.06E-05
	Ni	227828	0.026997	5.73E-05	1968	225860	0.026801	5.71E-05
	Cu	105277	0.012475	3.87E-05	972	104305	0.012377	3.86E-05
	Ga	5143	0.000609	8.50E-06	261	4882	0.000579	8.29E-06
	Co	2028	0.000240	5.34E-06	236	1792	0.000213	5.02E-06
748	Fe	369987	0.246780	4.53E-04	685	369302	0.246940	4.54E-04
	Pt	926061	0.617678	8.16E-04	1085	924976	0.618501	8.18E-04
	Ir	110296	0.073567	2.30E-04	339	109957	0.073524	2.30E-04
	Au	3170	0.002114	3.76E-05	80	3090	0.002066	3.72E-05
	Rh	17848	0.011905	8.96E-05	181	17667	0.011813	8.94E-05
	Ru	3927	0.002619	4.19E-05	290	3637	0.002432	4.04E-05
	Ni	38478	0.025665	1.33E-04	622	37856	0.025313	1.32E-04
	Cu	17051	0.011373	8.76E-05	307	16744	0.011196	8.70E-05
	Ga	11865	0.007914	7.29E-05	82	11783	0.007879	7.29E-05
	Co	578	0.000386	1.60E-05	75	503	0.000337	1.50E-05

ion count are the raw counts
ionic fraction is the raw count divided by the total counts
ionic fraction (sigma) is the estimated error
background count is the estimated background
background corrected values have had background count subtracted from the raw ion count

This is a preprint, the final version is subject to change, of the American Mineralogist (MSA)
Cite as Authors (Year) Title. American Mineralogist, in press.
(DOI will not work until issue is live.) DOI: http://dx.doi.org/10.2138/am-2015-4998

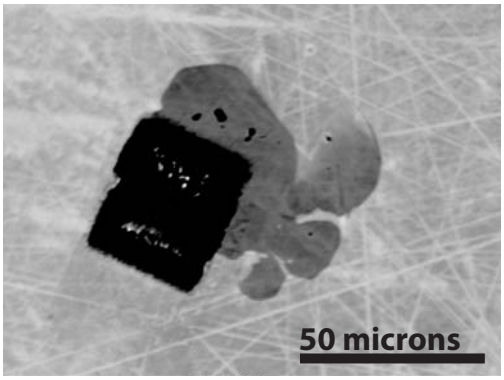

Figure 1. PtFe (darker gray) inclusions in osmiridium grain (lighter gray). Black square on edge of PtFe inclusion is FIB pit.

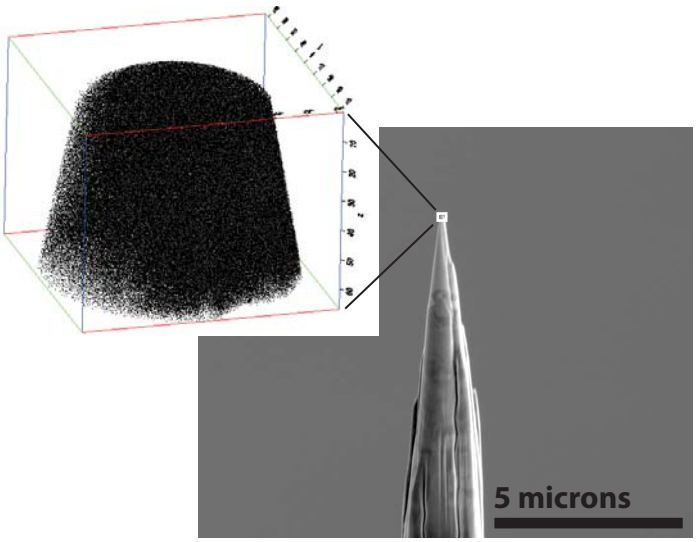

Figure 2. PtFe sample needle shaped with FIB. White box shows approximate area that was imaged during the APT analyses (~50 nm). Upper left image shows all 10 million atoms detected in perspective view.

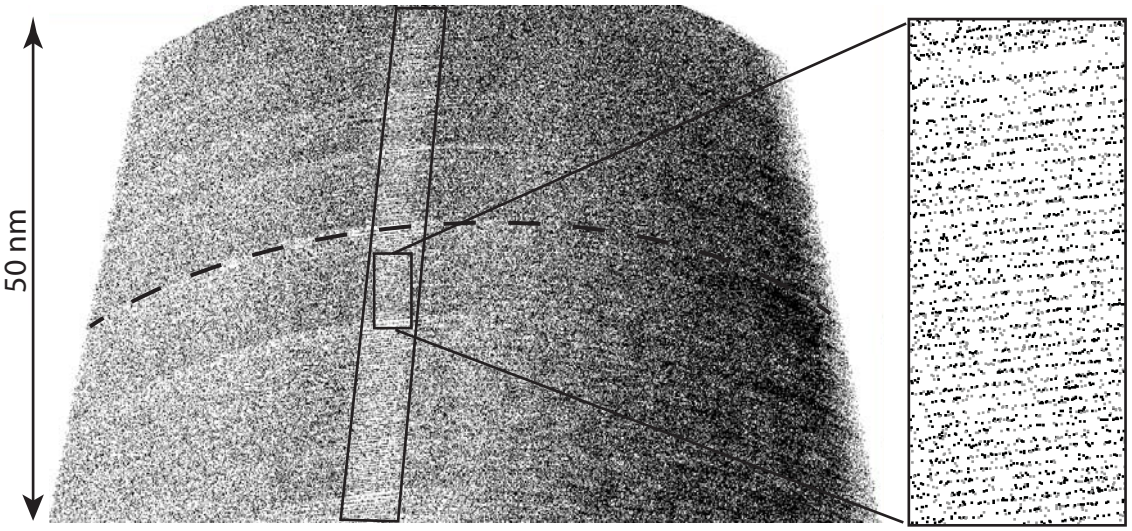

Figure 3. Pt and Fe atoms in alloy grain. The analysis volume is ~50 nm tall. The black dots are Pt and Fe atoms which constitute 88 mole% of the sample. The arcuate lines (highlighted by dashed line) in the reconstruction are an artefact of the bowl correction (see text for further discussion). Thin black line outlines volume where the imaging artefacts are minimized and atomic planes are resolvable (inset).

This is a preprint, the final version is subject to change, of the American Mineralogist (MSA)
Cite as Authors (Year) Title. American Mineralogist, in press.
(DOI will not work until issue is live.) DOI: http://dx.doi.org/10.2138/am-2015-4998

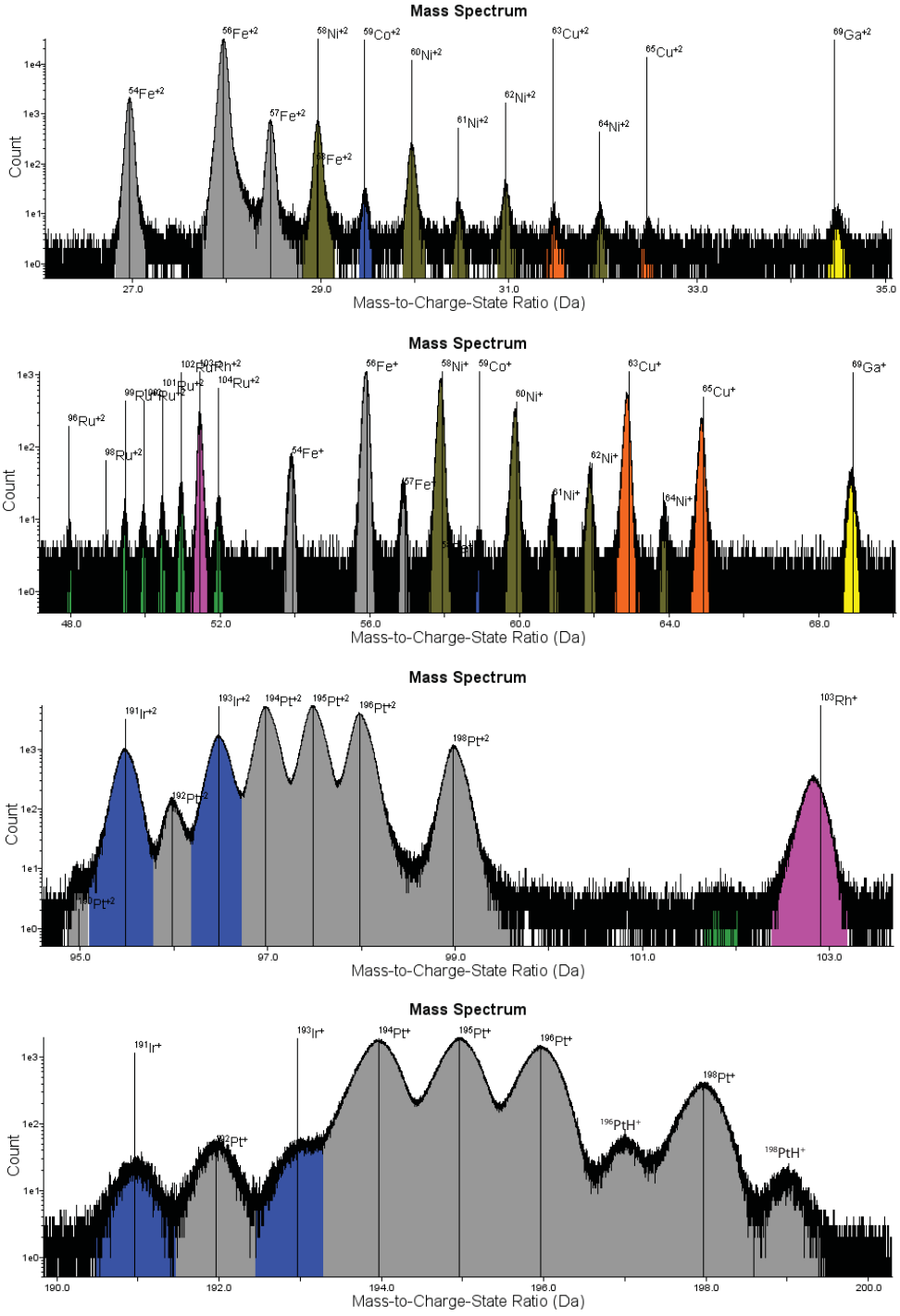

Figure 4. Mass/charge (m/q) spectra. Background for all peaks is less than 10 for the entire run (10 million counts, note log scale on y-axis). The symmetry of the peaks suggests there is little heating of the sample, which would produce asymmetric peaks skewed to higher m/q values (thermal tails). A small amount of PtH^+ is detectable and is included in the Pt concentrations.

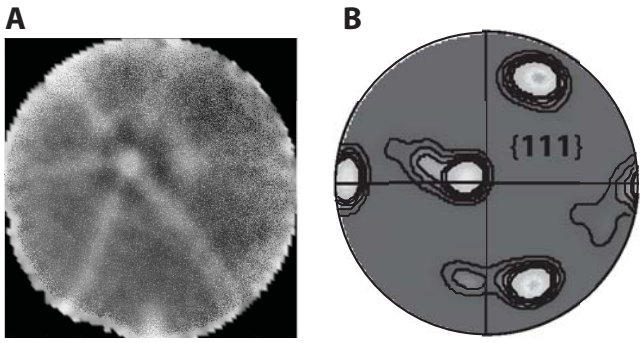

Figure 5. a) Histogram of number of atoms striking each pixel of the detector (darker = more detections). The hexagonally arranged white lines are low detection areas related to the crystal symmetry of the isoferroplatinum (hexagonal on the (111) plane). The white dot near the center is the {111} pole, which is 5° to the left of vertical. **b)** EBSD {111} pole figure showing {111} pole with the same 5° offset as in the histogram.

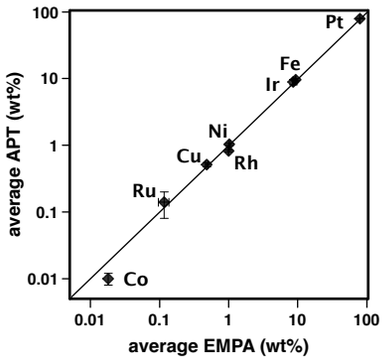

Figure 6. Elemental composition determined by APT compared to EMPA analysis. Error bars are 1 sigma standard deviation on 12 EMPA analyses. Cu was corrected for x-ray fluorescence from Os in the surrounding grain (see text). Values given in Table 1 and online Table 1.

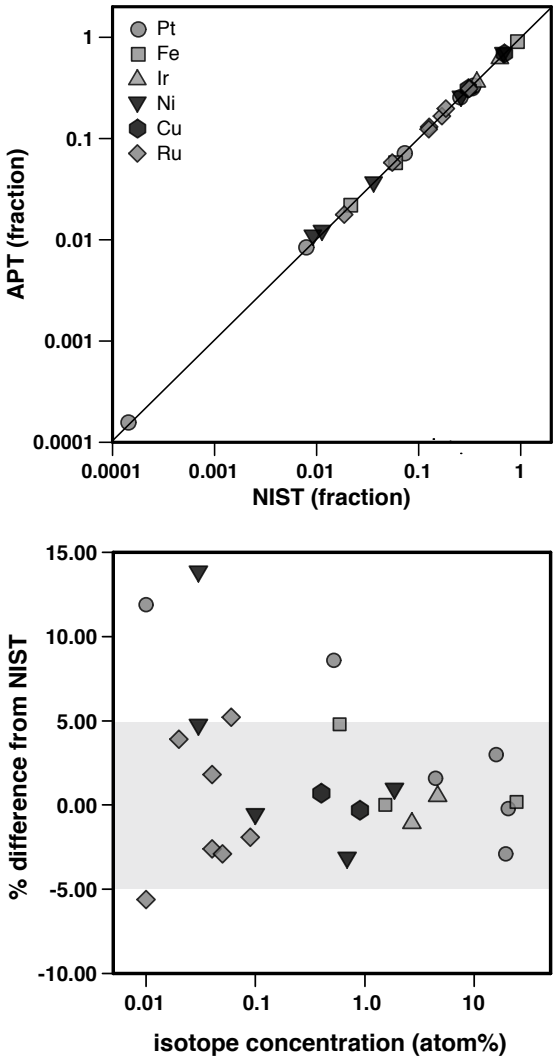

Figure 7. APT isotope analysis compared to published NIST values. **a)** atomic fraction of isotope (counts isotope/total counts element) determined by APT compared to values from NIST (Bohlke et al, 2005). b) % diffference between APT and NIST isotope fractions versus atomic concentration of isotope. The majority of isotope fractions are within 5% of the NIST values. Values given in Table 2 and online Table 2.

This is a preprint, the final version is subject to change, of the American Mineralogist (MSA)
Cite as Authors (Year) Title. American Mineralogist, in press.
(DOI will not work until issue is live.) DOI: http://dx.doi.org/10.2138/am-2015-4998

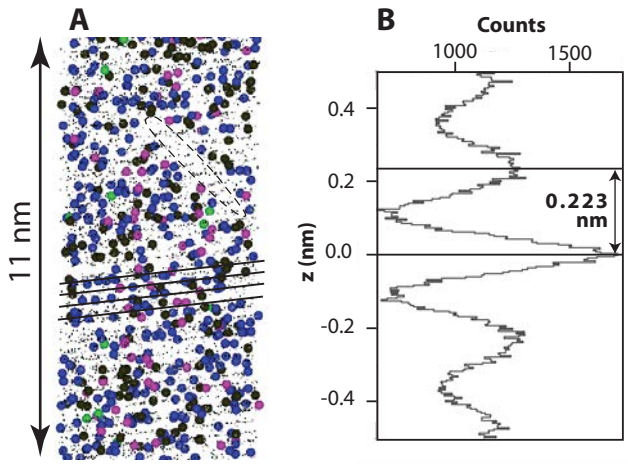

Figure 8. A) Locations of atoms: small dots are Pt and Fe, larger dots are minor elements (Ir, Ru, Rh, Cu, Ni, Co). Lattice planes (black lines) are 0.223 nm apart. Dashed ellipse outlines a region of PtFe that apparently is free of any other elements. **B)** Histogram of distances between atoms in the Z direction. Peak at 0.223 nm is the [111] lattice plane spacing.

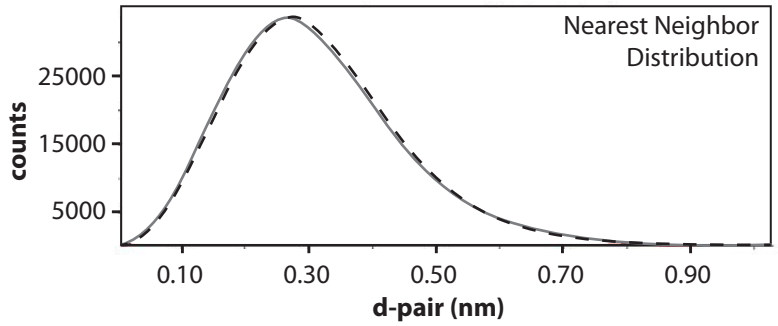

Figure 9. Nearest neighbor distribution between minor elements (Ir, Ru, Rh, Cu, Ni, Co). Gray line is observed distribution. Dashed line is a calculated random distribution. The similarity indicates there is no apparent clustering of atoms.